applied sciences

MDPI

Article

Theoretical Analysis of Directly Modulated Reflective Semiconductor Optical Amplifier Performance Enhancement by Microring Resonator-Based Notch Filtering

Zoe V. Rizou * and Kyriakos E. Zoiros

Lightwave Communications Research Group, Laboratory of Telecommunications Systems, Department of Electrical and Computer Engineering, Democritus University of Thrace, 67 100 Xanthi, Greece; kzoiros@ee.duth.gr

* Correspondence: zrizou@ee.duth.gr; Tel.: +30-25410-79-975

Received: 30 December 2017; Accepted: 28 January 2018; Published: 1 February 2018

Abstract: We demonstrate the feasibility of using a single microring resonator (MRR) as optical notch filter for enabling the direct modulation of a reflective semiconductor optical amplifier (RSOA) at more than tripled data rate than possible with the RSOA alone. We conduct a thorough simulation analysis to investigate and assess the impact of critical operating parameters on defined performance metrics, and we specify how the former must be selected so that the latter can become acceptable. By using an MRR of appropriate radius and detuning, the RSOA modulation bandwidth, which we explicitly quantify, can be extended to overcome the RSOA pattern-dependent performance limitations. Thus, the MRR makes the RSOA-encoded signal exhibit improved characteristics that can be exploited in practical RSOA direct modulation applications.

Keywords: direct modulation; microring resonator; optical notch filter; reflective semiconductor optical amplifier

1. Introduction

Reflective semiconductor amplifiers (RSOAs) are key modules for the realization of next-generation broadband access applications, such as colorless passive optical access networks [1], radio over fiber [2], slow and fast light [3], data erasing and remodulation [4], information packet power equalization [5] and fiber-optical cable television [6], which rely on the manipulation of data flowing in opposite directions. In effect, a single RSOA can simultaneously receive and amplify signals in the downstream while remodulating them with end-user information in the upstream communication link. This multifunctional capability is inherent to RSOAs, which owing to their internal structure use the same device facet both for signal input injection and output extraction. Thus, RSOAs avoid the need of having extra fiber paths, fiber components and optoelectronic elements to support bidirectional transmission, which helps reduce the overall system cost and complexity. However, as a physical byproduct of semiconductor optical amplifiers' finite carrier lifetime [7], the modulation bandwidth, which scales inversely against this parameter [8], of these devices, including RSOAs, is limited to a few GHz. For this reason, an RSOA can be directly modulated by electrical data, which are encoded on a seeding continuous wave (CW) light, only up to speeds which are not sufficient for satisfying the increasing bandwidth needs of the target applications. In the effort to overcome this fundamental limitation towards enabling full-duplex and symmetrical RSOA-based data transfer, several promising options are available, which include electronic equalization [9], advanced modulation formats [10,11], specially designed RSOA package and driving circuitry [12,13], and optical notch filtering [14]. In particular, the latter has been widely exploited because of the simple configuration, cost-affordable implementation using off-the-shelf

components and passive nature of the underlying signal-equalization mechanism. Furthermore, it is not concerned with challenging issues of the three other alternatives, such as the sensitivity to fiber chromatic dispersion and the requirement of high-speed sophisticated electronics at the transmitter and receiver side, in the first; the inevitable complex signal generation and detection in the second; and the involvement of elaborate fabrication and integration processes in the third. In fact, the two first RSOA bandwidth-extension techniques have even been combined with optical equalization and benefited from its efficiency to further improve their performance [11,15,16]. Thus, different schemes that act as optical notch filters on RSOA-encoded outputs have been reported, such as the delay interferometer (DI) [17,18], the fiber Bragg grating (FBG) [19] and the arrayed waveguide grating (AWG) [20]. In the same technological category also fall schemes that have been applied on conventional directly modulated SOAs, such as the birefringent fiber loop (BFL), either alone [21], in cascade with another BFL [22] or assisted by an optical bandpass filter [23]; and the microring resonator (MRR) [24]. The MRR is a special form of powerful waveguides [25,26], and exhibits distinctive characteristics over the aforementioned types of employed filters. These include the structural simplicity, the ultra-compact size–which makes it amenable to integration with microelectronic fabrication processes–enhanced wavelength selectivity, fine-tuning capability and availability of different material systems with the potential of copackaging with the SOA in the same hybrid platform. These attributes render the MRR a mostly suitable solution for increasing the operating speed of directly modulated RSOAs as well. In this paper, we investigate and demonstrate, by means of theoretical simulation and analysis, the MRR potential for overcoming the RSOA limited modulation bandwidth and thus for being extended beyond classical filter-oriented applications. For this purpose, we apply the model proposed in [27] to theoretically describe the operation of an RSOA when directly modulated by an electrical data pattern, a task that we initiated within the frame of [28]. Unlike the usually followed modeling approach, which involves solving a set of coupled partial nonlinear differential equations with boundary conditions [29,30], and hence is computationally demanding, this reduced model has been formulated on the basis of valid assumptions and prior framework [31] in such way that it allows one to derive the encoded signal at the RSOA output from the solution of a single standard differential equation in the time domain. This fact greatly simplifies the computational complexity while still providing realistic and accurate results. In this manner, we have been able to explore the capability of the MRR to enhance the data rate at which the RSOA can be directly modulated with acceptable performance. We have thus confirmed that if the MRR critical parameters are selected as specified in this work, it is indeed possible to extend by more than three times the repetition rate of the encoded signal, with the latter exhibiting improved characteristics.

2. RSOA Direct Modulation Assisted by MRR-Based Notch Filtering

2.1. Configuration

The basic configuration of a directly modulated RSOA is shown in Figure 1. A CW signal of constant power, P_{CW}, is inserted in the RSOA. Concurrently, a radio frequency (RF) signal, which comprises non-return-to-zero (NRZ) data pulses, is superimposed to the RSOA DC bias current, I_{bias}, and induces, via the RSOA electrical impedance, a peak current offset, $\pm I_m$. Since the RSOA rear edge is highly reflective, the CW signal undertakes a double pass inside the active medium of length L, and when it exits from the RSOA front facet, which is highly antireflective, it has perceived the gain variations due to the modulated current. Normally, the CW signal at the RSOA output should bear the exact digital information of the applied electrical excitation in optical form. However, as the rate of direct modulation gets faster, this may not happen, as due to the RSOA limited modulation bandwidth, the performance of the directly modulated RSOA is progressively deteriorated by pattern effects and eventually becomes poor. Still, it is possible to enhance the RSOA direct modulation capability by means of optical notch filtering. For this purpose, the RSOA is connected to an MRR, which, as shown in Figure 1, is a waveguide shaped into a ring structure of radius R coupled to a bus waveguide with field transmission coefficient r.

By properly tailoring the MRR spectral response, the MRR can efficiently act as frequency discriminator on the encoded pulses and improve their quality. This is done by adjusting the wavelength separation between adjacent peaks or notches, or free spectral range (FSR), which is inversely proportional to the MRR radius, and wavelength offset, that is, detuning, $\Delta\lambda$, between the encoded signal spectral position, λ_{enc}, and the nearest transfer function (TF) transmission peak, while maximizing the MRR transfer function peak-to-notch contrast ratio (PNCR) through operating the MRR in the critical coupling regime, where the microring internal losses are equal to the coupling losses. In this manner, the MRR compensates for the inherently limited bandwidth of the RSOA, and mitigates the pattern-dependent impairments induced on the encoded pulses.

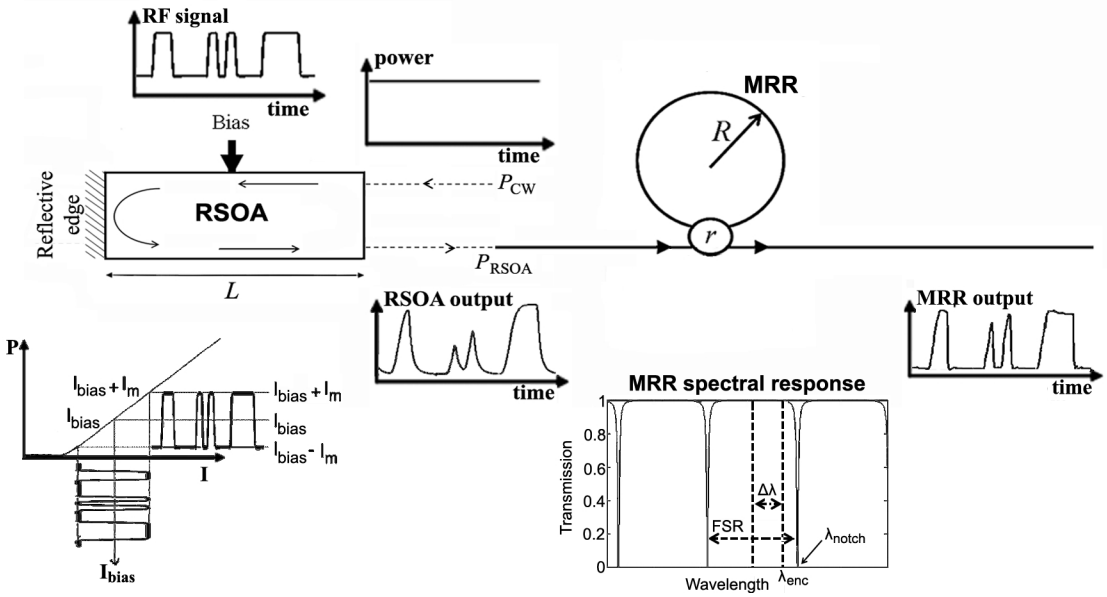

Figure 1. Conceptual view of reflective semiconductor amplifier (RSOA) direct modulation assisted by serially connected microring resonator (MRR). FSR: free spectral range, RF: radio frequency.

2.2. Modeling

The performance of the setup in Figure 1 is characterized by the power that emerges at the output of the directly modulated RSOA, $P_{RSOA}(t)$, and of the cascaded MRR-based notch filter, $P_{MRR}(t)$. This means that in order to simulate the operation of the scheme, it is necessary to know and calculate at each one of these points the lightwave-encoded signal electric fields, since they are normalized so that their squared modulus represents power, that is, $P_{RSOA,MRR}(t) = \left|E_{RSOA,MRR}(t)\right|^2$ [32].

For the RSOA case

$$E_{RSOA}(t) = \sqrt{P_{CW}}\exp\left[(1 - j\alpha_{LEF})h(t - 2Ln_g/c)\right], \tag{1}$$

where α_{LEF} is the RSOA linewidth enhancement factor, n_g is the group refractive index of the semiconductor material, c is the speed of light in vacuum, and the RSOA gain response integrated over its length is denoted by $h(t)$, which is shifted in time by twice the RSOA one-way transit time so as to account for the double pass taken by the lightwave signal within the RSOA optical cavity. Now, function $h(t)$ obeys the following one-dimensional differential equation [27]

$$\frac{dh(t)}{dt} = -\frac{h(t) - \Gamma a N_0 L\left[\dfrac{I(t)}{I_0} - 1\right]}{T_{car}} - \frac{\exp\left[2h(t)\right] - 1}{E_{sat}}P_{CW}, \tag{2}$$

where Γ is the RSOA confinement factor, a is the RSOA differential gain, N_0 is the RSOA carrier density at transparency, T_{car} is the RSOA carrier lifetime, $I_0 = qALN_0/T_{car}$ is the RSOA current at transparency (where q is the electron charge and A is the area of the semiconductor active region), and E_{sat} is the RSOA saturation energy. Equation (2) has been obtained after making the following valid assumptions and simplifications: (a) The RSOA internal losses are neglected, as they can be well compensated by the RSOA CW gain, G_{CW}, through the adjustment of the RSOA bias current, since these two parameters are directly related [27]; (b) the RSOA reflectivity is considered perfect, that is, 100%, as in practice this is a basic feature of the specific devices that favors their use [33], in particular as intensity modulators [10]; and (c) the RSOA round-trip propagation time, which is determined by the RSOA active region length, is smaller than the pulse repetition interval of the applied excitation. This condition is satisfied for the direct modulation rates pursued in RSOAs being less than 1 mm long [34].

The profile of each pulse inside the $N = 2^7 - 1$ bit-long NRZ pseudorandom binary sequence (PRBS) of the injection current is described in compact form [35,36] as the sum of a DC term and a modulation term

$$I(t) = \overbrace{(I_{bias} - I_m)}^{\text{DC term}} + \overbrace{2I_m\left\{H(t)\left[1 - \mathrm{e}^{-t^2/t_r^2}\right] - H(t-T)\left[1 - \mathrm{e}^{-(t-T)^2/t_r^2}\right]\right\}}^{\Delta\mathrm{I(t)} \equiv \text{ modulation term}}, \quad (3)$$

where $H(t)$ is Heaviside step function, I_{bias} and I_m are the RSOA bias current and induced RF modulation current, respectively–which are a small fraction of the current at transparency–and t_r is the pulse rise time, which occupies a small portion of the pulse repetition period, T.

For the MRR case, obtaining the electric field at its output involves the following steps. First, the RSOA temporal response is extracted by numerically solving for $h(t)$ from (2). This is done by following the numerical method formulated in [37] but adapted to account for a temporal-dependent total injection current [38]. More specifically, for each information bit of duration T carried by the modulation current, (2) is solved in a step-wise manner by approximating the time derivative of $h(t)$ by a finite difference and applying the appropriate initial conditions. For this purpose, the continuous time variable t is replaced by discrete points $t_{p,i} = (p-1)T + i\Delta t$, for $p = 1, 2, \ldots, N$ and $i = 1, 2, \ldots, k$, where p denotes the p-th pulse inside the N-long PRBS of the injection current, Δt is the finite temporal increment and $k = T/\Delta t$ is the integer number of calculated samples of function $h(t)$ in each bit period. To ensure high enough temporal resolution and at the same time enhanced computational efficiency so as to correctly capture the RSOA gain dynamics expressed by $h(t)$ with affordable hardware and software resources, we choose $\Delta t = 1$ ps, which means that nearly 100 samples are taken at all data rates considered in this paper. Then, the knowledge of $h(t)$ and of its derivative at a given pulse instant "i", $h_{p,i}$ and $dh_{p,i}/dt$, respectively, allows one to calculate the value, $h(t + \Delta t)$, at the next discrete moment, $h_{p,i+1}$, according to Euler's numerical method. This method is suitable for studying the response of semiconductor active waveguide devices, such as the RSOA, to an electrical excitation of piecewise varying nature, such as the injection current NRZ pulses, as it converges rather fast while producing reasonable results [39]. The initial conditions required for running this process are (a) $h_{1,1} = \bar{g}_0 L$, where $\bar{g}_0 = \Gamma a N_0 \{[(I_{bias} - I_m)/I_0] - 1\}$ is the RSOA steady-state gain coefficient. This condition is a direct byproduct of the fact that the first temporal segment in the leading edge of the very first information pulse, which is assumed to be a mark and is supplied to the RSOA through the injection current pulse stream, experiences an unsaturated RSOA gain, since the carriers of the latter have not had the time to be modified yet; (b) $h_{p,1} = h_{p-1,k}$, to account for the fact that the gain available to the first temporal segment in the leading edge of every next pulse is that left by the last temporal segment of the immediately preceding pulse. This condition is properly adapted and reduced to the case of consecutive NRZ pulses carrying the same binary information, that is, strings of marks or spaces. This process is carried out iteratively until all $N \cdot k$-th values of $h(t)$ are obtained, which can be

then stored in a matrix and retrieved for further calculations. The solution for $h(t)$ is then substituted in (1) to find the electric field of the encoded signal at the RSOA output. This function is transferred then into the frequency domain and is convolved with the MRR spectral response. The latter has the compact mathematical expression given below [40],

$$T_{MRR}(\lambda) = \frac{r - l\exp\left[jn_{eff}4\pi^2R\left((\lambda-\Delta\lambda)/\lambda^2\right)\right]}{1 - rl\exp\left[jn_{eff}4\pi^2R\left((\lambda-\Delta\lambda)/\lambda^2\right)\right]}, \tag{4}$$

where n_{eff} is the waveguide effective refractive index while the field transmission coefficient, r, and amplitude attenuation factor, l, are equal and tend to unity so as to ensure that the MRR is operating in the critical coupling regime [41] where it can efficiently act as notch filter [42]. Then, the convolution product is converted back into the time domain. This procedure can be put in mathematical form as $E_{MRR}(t) = \mathcal{F}^{-1}\{\mathcal{F}\left[E_{SOA}(t)\right]T_{MRR}(\lambda)\}$, where operators, $\mathcal{F}\{\cdot\}$ and $\mathcal{F}^{-1}\{\cdot\}$ denote fast Fourier transform (FFT) and inverse FFT, respectively, which are both available and executed in Matlab software. Therefore, $P_{MRR}(t) = |E_{MRR}(t)|^2$. In this manner, the maximum and average values of the peak power of the marks and spaces within the encoded PRBS can be found so that they can be used to calculate the performance metrics employed in the following section.

The operation of the directly modulated RSOA, either alone or assisted by the MRR, is also characterized by the respective modulation responses, which are derived through the process of small-signal analysis [43,44]. Starting with the RSOA, we have

$$T_{RSOA} \overset{①}{=} \frac{p_{RSOA}(\Omega_m)}{p_{RSOA}(0)} \overset{②}{=} \frac{\Delta h(\Omega_m)}{\Delta h(0)} \overset{③}{=} \frac{\Delta g(\Omega_m)D(0)}{\Delta g(0)D(\Omega_m)}, \tag{5}$$

where the expressions that follow after steps ①, ② and ③ have been derived by combining relevant information from [18,27] and [45] (c.f. Appendix). More specifically, in ①, $p_{RSOA}(\Omega_m)$ is the small-signal power, which is produced at the RSOA output due to the modulation of its current at a given frequency, $f_m = \Omega_m/2\pi$, and normalized over its unmodulated counterpart [46]; in ②, $\Delta h(\Omega_m)$ is the concomitant small-signal deviation from steady state of the RSOA-integrated gain given by [27] $\Delta h(\Omega_m) = [L/D(\Omega_m)]\Delta g(\Omega_m)$, where $\Delta g(\Omega_m) = \Gamma a N_0 \Delta I(\Omega_m)/I_0$ is the corresponding gain coefficient perturbation incurred by the modulation current of complex envelope $\Delta I(\Omega_m)$; and in ③, $D(\Omega_m) = 1 - j\Omega_m T_{car} + W\left[\frac{2T_{car}P_{CW}}{E_{sat}}\exp\left(2\bar{g}_0 L + \frac{2T_{car}P_{CW}}{E_{sat}}\right)\right]$ [27], where $W[\cdot]$ is Lambert's 'W' function [47]. Function $D(\Omega_m)$ links in a compact manner the perturbation of the RSOA-integrated gain to the current modulation from which it has been incurred. Thus, when the RSOA is directly modulated by a sinusoidal electrical excitation, it allows, through first-order approximations, one to analytically express the 3 dB angular frequency of the RSOA modulation response as [27] $\Omega_{3dB} = \frac{\sqrt{3}}{T_{car}}\left\{1 + W\left[\frac{2T_{car}P_{CW}}{E_{sat}}\exp\left(2\bar{g}_0 L + \frac{2T_{car}P_{CW}}{E_{sat}}\right)\right]\right\}$. This formula provides an estimate of the maximum RSOA modulation frequency and hence of its direct modulation capability at a given data rate [28]. In general, however, the modulation current may be in digital form and have any shape. Then, the 3-dB modulation bandwidth can be derived from (5) by taking the Fourier transform of the modulation current in the time domain, which in our case is given by the second term in the right-hand side of (3). By using Fourier transform formulas and properties of the functions involved therein, and after tight algebraic manipulations, in the course of which the complementary error function and the imaginary error function come into being, we find the explicit expression

$$\begin{aligned}&\Delta I(\Omega_m) = \mathcal{F}[\Delta I(t)] = \\ &= 2I_m\left\{\tfrac{1}{j\Omega_m}\left[1 - \exp(-j\Omega_m T)\right] + \left[\exp(-j\Omega_m T) - 1\right]\left[0.5\sqrt{\pi}t_r\exp\left(-\Omega_m^2 t_r^2/4\right) - jt_r\mathbb{F}(\Omega_m t_r/2)\right]\right\},\end{aligned} \tag{6}$$

where function $\mathbb{F}(x) = \exp(-x^2)\int_0^x \exp(t^2)dt$ represents Dawson's integral [48], which is available in Matlab software. Taking the squared modulus and after proper algebraic manipulations, (6) can be brought into a form that allows one to approximate its values for the boundary conditions of the modulation frequency [46]. The obtained result is analogous to the square of the product of the electrical modulation pulses' peak amplitudes and period when $\Omega_m \to 0$, while it tends to null when $\Omega_m \to \infty$. In other words, the level of the specific function in these two limits is in the opposite direction to that of the modulation frequency variation. This fact confirms that the RSOA modulation response exhibits a low-pass characteristic, which is in agreement with the same trend noticed from extensive numerical calculations [49].

For the MRR, on the other hand, the modulation response is [24]

$$\begin{aligned} T_{MRR} &= A \times \left((1 - j\alpha_{LEF})/2\right) \times \frac{A^* + \Omega_m^2 + 2\delta\Omega_m + j\mu_e^2\Omega_m}{\delta^2\left((\delta+\Omega_m)^2 + 1/\tau^2\right)} + \\ &+ A^* \times \left((1 + j\alpha_{LEF})/2\right) \times \frac{A + \Omega_m^2 - 2\delta\Omega_m + j\mu_e^2\Omega_m}{\delta^2\left((\delta-\Omega_m)^2 + 1/\tau^2\right)}. \end{aligned} \tag{7}$$

In this expression, $A = \delta^2 - j\mu_e^2\delta$ (and A^* is the complex conjugate), $\delta = 2\pi c\dfrac{\lambda_{notch} - \lambda_{enc}}{\lambda_{notch}\lambda_{enc}}$, where λ_{notch} is the spectral position of the MRR transfer function notch (Figure 1) that obeys the condition of MRR resonance, $2\pi R n_{eff} = m\lambda_{notch}$, $m \in Z^*$, and lies nearest to the encoded optical signal of wavelength, λ_{enc}, in the vicinity of 1550 nm, and μ_e is the coupling strength between the bus waveguide and the ring, $\mu_e^2 = \left[(1 - r^2)c/2\pi R n_{eff}\right] = 1/\tau$, where the last equality with the MRR $1/e$ amplitude decay time, τ, holds under critical coupling [44]. The modulation response of the MRR-assisted RSOA is then obtained by taking the absolute value of (5) and multiplying it with the modulus of (7).

Finally, an inevitable consequence of RSOA direct modulation is that the encoded pulses acquire an instantaneous frequency deviation, that is, chirp, across them [50]. The compensation of the chirp's irregular temporal variation via post-optical notch filter is converted by the latter to restored quality of encoded pulses and accordingly enhanced RSOA modulation capability. This means that quantifying this transient effect can also provide useful information for the operation and performance of the MRR-assisted directly modulated RSOA. For this purpose, the knowledge of the phase response of the RSOA and MRR is required since the chirp, $\Delta v(t)$, is by definition linked to it through the derivative in the time domain [51]. Finding the chirp for the SOA case is straightforward by isolating the output phase term from (1), differentiating it in time and readily taking the differential of the time-delayed version of the RSOA-integrated gain response from the right-hand side of (2) using the transform $t \to t - 2Ln_g/c$. For the MRR case, however, the phase of the transmitted light undergoes a steep variation around resonance [52], which compromises the direct numerical calculation of the corresponding response and accordingly of its temporal rate of change, which provides the chirp. Instead of taking the inverse tangent function of the ratio between the imaginary and real parts of the complex-valued electric field [53], we use the relevant information that is extracted when applying the signal phase-reconstruction technique in the optical domain [54,55]. This technique allows one to unambiguously recover the instantaneous frequency deviation profile of a random repetitive data signal which is inserted in a frequency discriminator whose spectral transfer function has a linear spectral amplitude variation around the detuning position. This element acts as a differentiator on the inserted signal, which is exactly what the MRR-based notch filter does in our case [52]. In this manner, the desired chirp can be directly extracted in analytical form from the knowledge of the time-domain intensity profiles of the signals that enter and exit the MRR. Thus [54],

$$-2\pi\Delta v_{MRR}(t) = -\sqrt{\frac{1}{|E_{RSOA}(t)|^2}\cdot\left[\left(\frac{|E_{MRR}(t)|}{S}\right)^2 - \left(\frac{\partial|E_{RSOA}(t)|}{\partial t}\right)^2\right]} + \delta, \tag{8}$$

where S is the slope of the linear amplitude variation around the detuning point of the MRR TF with respect to angular frequency, which can be found by differentiating (4) and applying the chain rule [56].

3. Results

We found first if and how the RSOA can be directly modulated on its own without performance degradation. For this purpose we investigated the impact of the parameters associated with the optical and electrical RSOA excitation signal on the error probability (EP) which, for acceptable performance, should not exceed the forward error correction (FEC) threshold of 3.8×10^{-3} [22,24]. The error probability is analytically extracted through the Q-factor, which is defined as

$$Q = \frac{\bar{P}_1 - \bar{P}_0}{\sigma_{1,pe} + \sigma_{0,pe}}, \tag{9}$$

where $\bar{P}_1$, $\bar{P}_0$ are the mean and $\sigma^2_{1,pe}$, $\sigma^2_{0,pe}$ are the variances of the peak power of encoded marks ('1's) or spaces ('0's), respectively, which are numerically computed according to the details provided in the previous section, in the presence of pattern effects manifested due to the RSOA direct modulation (hence the subscript 'pe'). Because the amplitude distortions incurred by these effects on the encoded bits at the RSOA output are intense, the variances in the denominator of (9) dominate over the variances of conventional noise components, such as those associated with the RSOA amplified spontaneous emission (ASE) [30]. Moreover, given that the statistics of these distortions follow the Gaussian distribution [30], the relationship between the EP and the Q-factor reads [57]

$$EP = \frac{1}{2}\text{erfc}\left(\frac{Q}{\sqrt{2}}\right), \tag{10}$$

where erfc(.) is the complementary error function.

Figure 2 shows the EP versus the RSOA CW input power and bias current for three different direct modulation rates. This figure has been obtained for the RSOA structural and physical parameter values employed or derived in [28]. The values of the total injection current characteristics that have been used in deriving Figure 2a are $I_{bias} = 1.2I_0$ and $I_m = 0.1I_0$, where the current at transparency is ~75 mA and $t_r = 17\%T$. On the other hand, Figure 2b has been obtained for a CW input power of -10 dBm. The EP is acceptable for all scanned parameters' range at 2.5 Gb/s, but as we go to 3 Gb/s and beyond, it is necessary to provide more CW power and bias current. The physical explanation for this behavior of the EP is that the increase of the RSOA driving optical power and applied electrical bias accelerates the RSOA response [10] and widens its modulation bandwidth [58], so that the RSOA is allowed to handle data of higher rate. According to this fact, the continuous increase of the examined parameter values would seem natural for supporting faster RSOA direct modulation. However, there are physical limitations in this trend, which are imposed by the RSOA CW gain and the maximum amplitude difference, that is, extinction, between marks and spaces, $AD_{1/0,max}$ [24]. In fact, increasing too much the CW power forces the RSOA to enter into the deep saturation regime where it provides a reduced optical gain, while increasing too much the bias current shifts the RSOA electrical modulation to occur beyond the linear gain–current region, that is, into the hard limit where the information-driving current is made to experience an almost flat RSOA optical gain [58]. For these physical reasons, the electrical current-induced RSOA optical gain perturbation conditions become such that they degrade the encoded output quality due to the modulated signal's decreased extinction in the first case and increased clipping in the second one.

The CW gain should not fall below 10 dB so that the encoded signal, after undergoing the subsequent filtering action, can still have enough power to be used in RSOA direct modulation applications [13]. $AD_{1/0,max}$ should exceed 10 dB [13] so that the encoded marks are sufficiently distinguished from the encoded spaces.

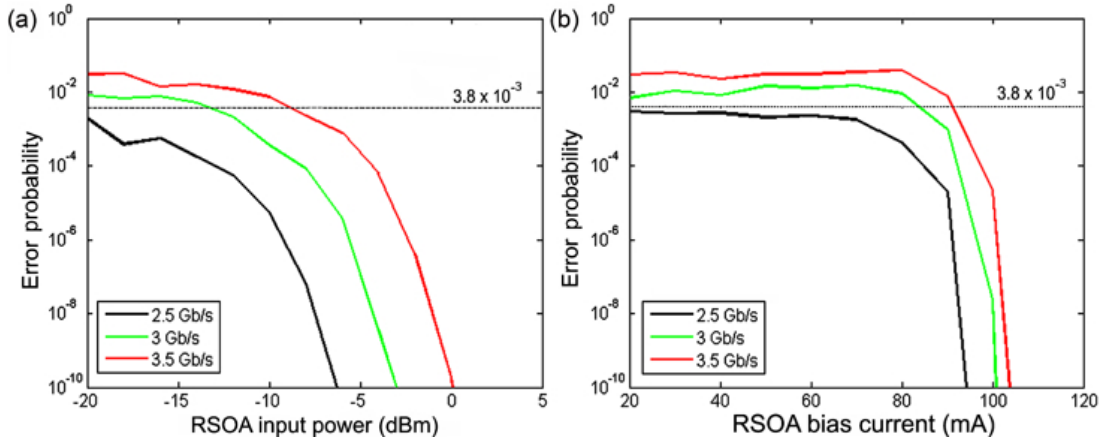

Figure 2. Error probability at RSOA output versus RSOA (**a**) input power and (**b**) bias current. The horizontal dotted line denotes the FEC limit.

Then, from Figures 3 and 4 it can be observed that these requirements can simultaneously be satisfied for some input power and bias current values only up to 3 Gb/s. Thus, an appropriate combination of these parameters is $P_{CW} = -12$ dBm and $I_{bias} = 90$ mA, for which $EP = 4.3 \times 10^{-3}$, CW gain = 12.05 dB and $AD_{1/0,max} = 10.02$ dB.

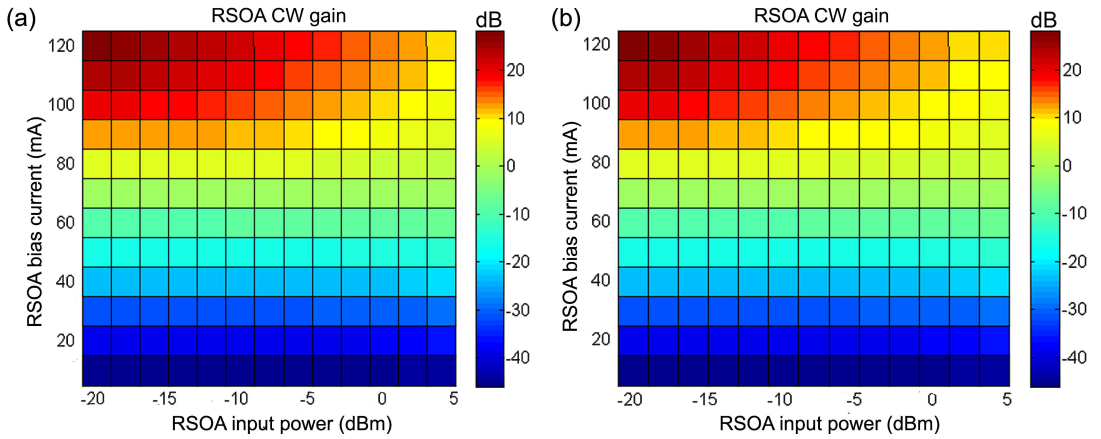

Figure 3. RSOA continuous wave (CW) gain versus RSOA input power and bias current at (**a**) 3 Gb/s and (**b**) 3.5 Gb/s.

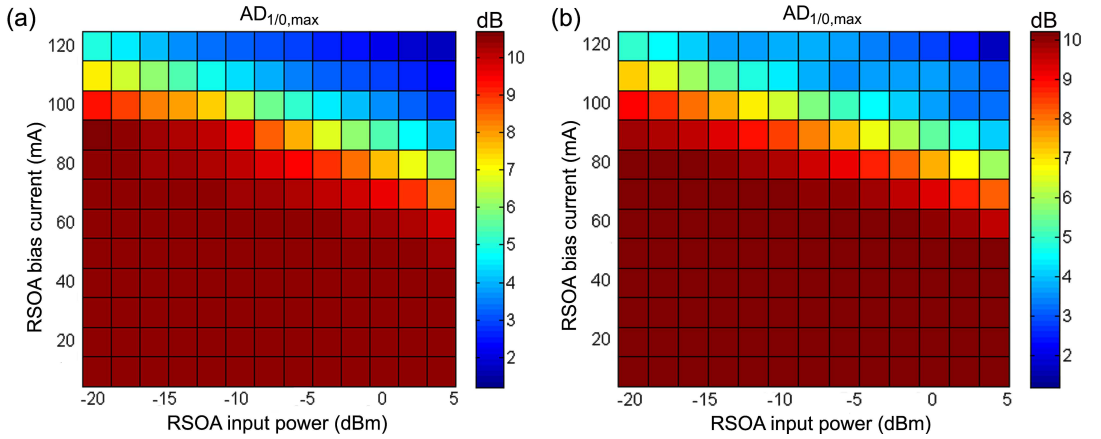

Figure 4. $AD_{1/0,max}$ versus RSOA input power and bias current at (**a**) 3 Gb/s and (**b**) 3.5 Gb/s.

The suitability of this choice is also confirmed by the resultant RSOA modulation bandwidth, which, as shown in Figure 5, is of the order of 3 GHz and hence consistent with the above findings.

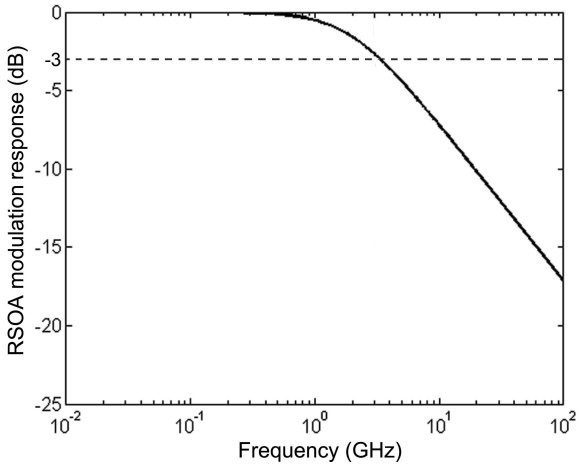

Figure 5. RSOA modulation response for input power −12 dBm and bias current 90 mA.

On the other hand, Figure 6 shows that the RSOA direct modulation capability is not affected by the injection current modulation amplitude and rise time since, despite their variation, the RSOA modulation bandwidth remains nearly the same. Physically this happens because the RSOA operating conditions set by the specified CW power and bias current are such that the negative effects of encoded signal extinction ratio degradation and amplitude clipping are appropriately balanced so that they become rather independent of the modulation current peak and rise time.

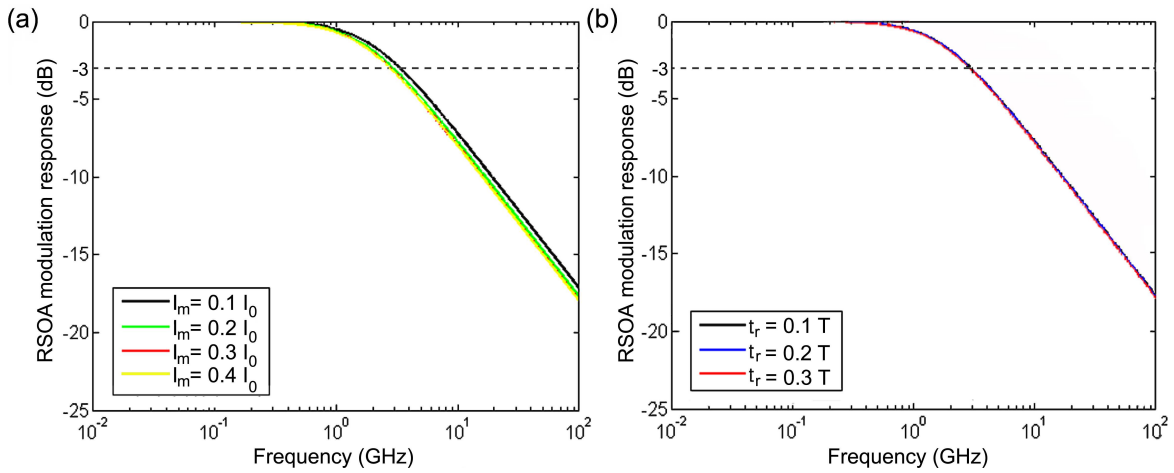

Figure 6. RSOA modulation response for different (**a**) peak modulation currents and (**b**) modulation current rise times.

Figure 7 compiles the encoded pulse waveforms, chirp and pseudo-eye diagrams (PEDs) for favorable (top) and adverse (bottom) RSOA direct modulation which occur at 3 Gb/s and 5 Gb/s, respectively. These opposing cases can be quantitatively compared not only against the EP but also against the maximum amplitude difference between marks, $AD_{1,max}$, and $AD_{1/0,max}$ [24], red chirp fluctuations (CF) [59] and PED eye opening (EO) [24]. Thus, $EP = 4.3 \times 10^{-3}$ at 3 Gb/s vs. 7.6×10^{-2} at 5 Gb/s, $AD_{1,max} = 0.22$ dB at 3 Gb/s vs. 1.03 dB at 5 Gb/s, $AD_{1/0,max} = 10.02$ dB at 3 Gb/s vs. 8.1 dB at 5 Gb/s, $CF = 2\%$ at 3 Gb/s vs. 15% at 5 Gb/s and $EO = 87\%$ at 3 Gb/s vs. 72% at 5 Gb/s.

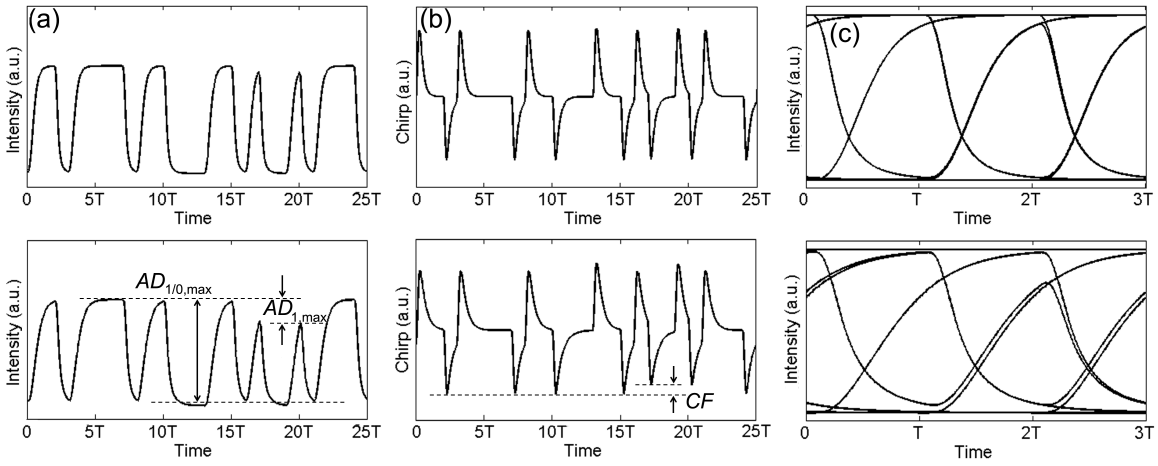

Figure 7. RSOA-encoded pulses (**a**) waveform, (**b**) chirp and (**c**) pseudo-eye diagram at 3 Gb/s (top) and 5 Gb/s (bottom).

A passive single-bus MRR employed as notch filter can allow one to directly modulate the RSOA at enhanced data rate with acceptable performance. To this aim, we must properly select the MRR radius and detuning, and Figure 8 depicts the EP versus these parameters for three different RSOA direct modulation rates which are at least three times higher than the maximum data rate being possible for the RSOA alone. For acceptable performance, not only the EP should lie below the defined FEC limit, but also $AD_{1,max}$ should be below 1 dB [60], $AD_{1/0,max}$ over 10 dB [13], CF should tend to unity, or equivalently 0%, so that the phase variation per time increment of the encoded pulses is as balanced as possible [61], while the overshoot (OS) that inevitably manifests on the encoded pulses [22] should be kept within 25% [62]. The MRR key parameter specifications that efficiently account for, and compromise between, these conditions so that all metrics are acceptable up to 11 Gb/s are $R \in \{8, 12, 16, 20\}$μm and $\Delta\lambda = 0.67$ nm $\pm$ 0.02 nm. These specifications have been derived by combining information from the results obtained both graphically (EP) and numerically ($AD_{1,max}$, $AD_{1/0,max}$, CF, OS). The existence of a specific permissible range of values for both MRR radius and detuning is physically attributed to the conditions that must be fulfilled for the MRR-based filter to efficiently mitigate the pattern-dependent impairments of the directly modulated RSOA. This requires the MRR to properly act upon the encoded pulses spectrum, which due to the RSOA direct modulation has been modified in accordance with the binary content and position of each pulse. For this purpose, the MRR transmission properties must be suitably tailored, which involves choosing and controlling the wavelength spacing (FSR) as well as the contrast and the position of the notches, by following and fulfilling the necessary conditions. The general guidelines are that: (a) The FSR must be adjusted by taking into account the trade-off between the margin of the TF spectral border, which is defined by the difference between the reference data and the nearest notch wavelength, the TF passband width, the spectral components' suppression degree dependence on pulse peak amplitude they originate from, and the optical carrier level of transmission after filtering; (b) the repetitive notches must be sharp and deep enough to maximize their magnitude difference from their adjacent transmission peaks, which defines the PNCR; and (c) the notches must occur at a longer wavelength than that of the encoded signal so that the MRR transmittance is decreased as the wavelength is increased.

The beneficial effect of an MRR with optimum radius and detuning $R = 20$ μm and $\Delta\lambda = 0.65$ nm, respectively, or $\simeq$ FSR/20, which fall within the range of permissible values specified above, on the encoded signal characteristics at 11 Gb/s is shown in the lower part of Figure 9, where for comparison the same results for the RSOA only are depicted in the upper part. The obtained performance metrics are $EP = 3.56 \times 10^{-4}$ (MRR) vs. 2.86×10^{-1} (RSOA), $AD_{1,max} = 0.64$ dB (MRR) vs. 3.32 dB (RSOA), $AD_{1/0,max} = 10.63$ dB (MRR) vs. 5.88 dB (RSOA), $CF = 9\%$ (MRR) vs. 48% (RSOA), $EO = 87.4\%$ (MRR) vs. 44.5% (RSOA) and $OS = 8\%$. In addition, the net gain (NG) of the RSOA–MRR system [51]

is 6.54 dB, thus being exploitable for direct modulation purposes [24]. This value can be increased to approach 10 dB provided that the coupling coefficient, r, tends closer to unity, since in this case the creation of the MRR spectral response, according to the general guidelines mentioned above for efficiently mitigating the pattern-dependent impairments of the directly modulated RSOA, is favored. Still, such choice of the specific parameter is practically compromised by the tighter adjustments related to the gap between the straight and bending waveguides. On the other hand, varying the MRR radius from the maximum to the minimum permissible value specified for this parameter does not improve the NG. In fact, this action increases the FSR, which in turn makes the slope of the MRR transfer function less steep. This increases the likelihood that the amplified optical carrier will fail to fall close to the transmission peak, thus suffering by the MRR a greater attenuation of its intensity, which results in less available NG.

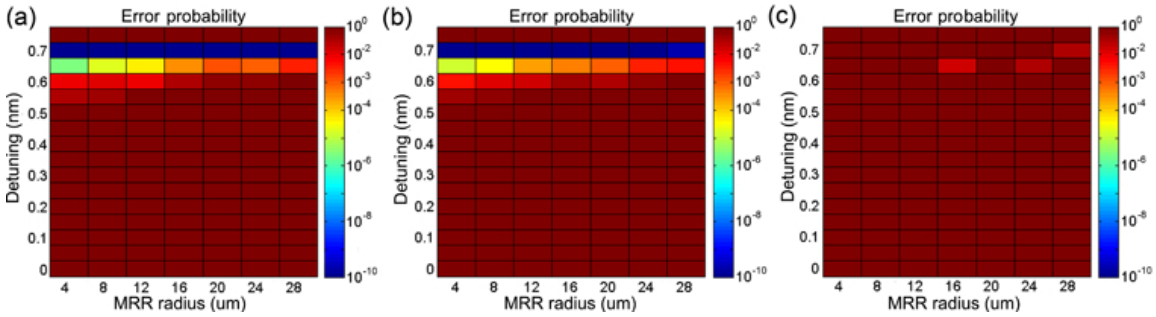

Figure 8. Error probability at MRR output for different MRR radii and detuning at (**a**) 10.5 Gb/s, (**b**) 11 Gb/s and (**c**) 11.5 Gb/s.

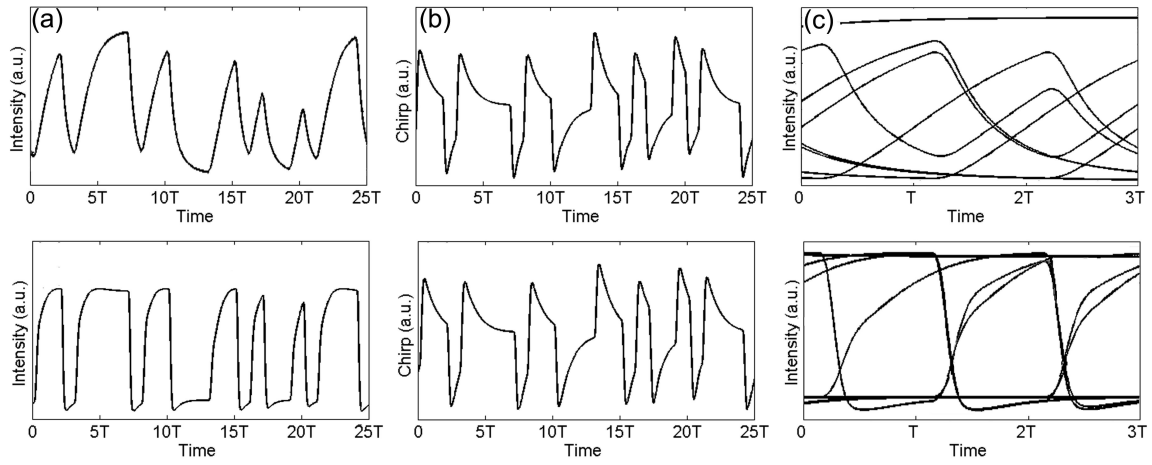

Figure 9. RSOA output (top) and MRR output (bottom) encoded pulses (**a**) waveform, (**b**) chirp and (**c**) pseudo-eye diagram at 11 Gb/s.

Figure 10 shows that owing to the MRR, the RSOA modulation bandwidth is extended indeed to 11 GHz. The peaking observed in the modulation response is induced by the MRR transient time dynamics and is the physical result of interference between the light that circulates inside the ring and the light inserted in the bus waveguide from the RSOA [63]. Consequently, its magnitude should depend on the fraction of the power that comes from the RSOA and enters the ring, that is, $(1 - r^2) \times 100\%$. Our simulations conducted in the critical coupling regime thus show that when this quantity is 9.75%, the frequency position of peaking is shifted to its maximum, which however is not exploitable for RSOA direct modulation at the corresponding data rate due to the constraints imposed by EP, $AD_{1,max}$, $AD_{1/0,max}$, CF and OS. In contrast, when the percentage of coupled power drops to ~2%, the peaking can be leveraged for enhancing the RSOA modulation

bandwidth to an extent that is determined approximately by the detuning between the encoded signal and the MRR notch at resonance, that is, $\approx \delta/2\pi$ [24]. On the other hand, according to the above justification for the appearance of peaking, the latter is not affected by changes in the ring radius values, which alter the order of resonance but not the spectral position of the notch. This happens in our case, since the derived permissible values of the MRR radius follow this pattern by being integer multiples of 4 μm. From a mathematical perspective, this leaves intact the parameter δ and accordingly the degree of peaking.

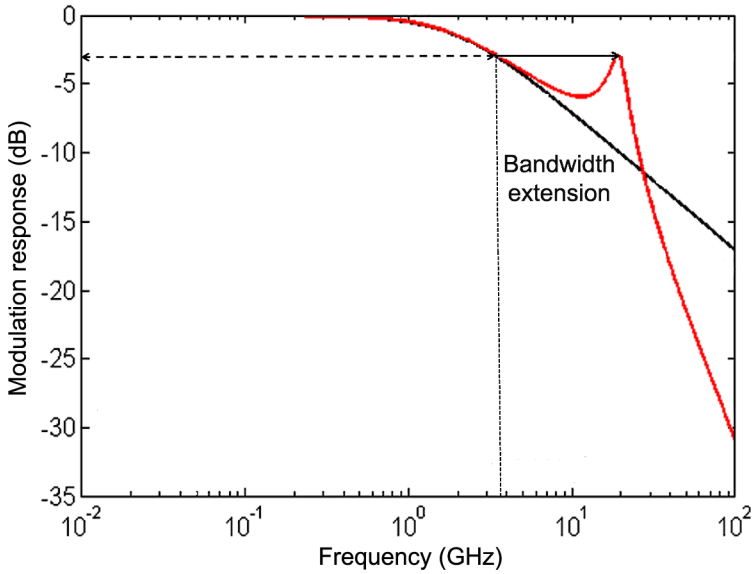

Figure 10. Modulation response of RSOA alone (black line) and with the addition of MRR (red line).

Finally, Figure 11 depicts the MRR transfer function and its impact on the spectral components of the maximum and minimum logical '1's and '0's within the RSOA-encoded data stream. According to [24], it can be seen that the spectral peaks of the encoded logical '1's are shifted to the longer sideband relative to the optical carrier, while those of the encoded logical '0's are shifted to the shorter sideband. In order to combat the deleterious consequences of RSOA direct modulation provoked by the limited RSOA modulation bandwidth, the spectral peaks of the encoded '1's must lie in the falling slope of the MRR TF, with the peak of the maximum '1' being located closer to the TF notch than the peak of the minimum '1', so that the MRR transmits the former less than the latter. Moreover, the spectral peaks of the encoded logical '0's must be confined around the flat portion of the MRR TF, with the peak of the minimum '0' being located nearer to the MRR TF transparency point than the peak of the maximum '0', so that the MRR favors the former more than the latter. These requirements are efficiently satisfied by using the specified optimum parameters of the MRR, whose spectral response figures-of-merit thus are [40] $FSR = \lambda_{enc}^2/(2\pi n_{eff} R) = 13.5$ nm, resonance peak full-width at half-maximum $FWHM = \lambda_{enc}^2(1 - rl)/(2\pi^2 n_{eff} R\sqrt{rl}) = 0.44$ nm and finesse $F = FSR/FWHM = 31$, which have been calculated by substituting $\lambda_{enc} = 1550$ nm, $n_{eff} = 1.41$, $R = 20$ μm, and $r = l = 0.95$ so that the PNCR is ideally infinite. Then, the MRR can act upon the spectral components of the encoded pulses so that the peak differences can become more even for pulses of the same binary content, that is, '1's vs '1's or '0's vs '0's, and more distinguishable between pulses of different binary content, that is, '1's vs '0's. In addition, the absolute magnitudes of marks and spaces can become more enhanced and suppressed, respectively. In this manner, the MRR transforms the pattern-dependent distortions, which have been mapped on the encoded signal's spectral components, into pulse amplitude variations [15] that cancel those present right after the directly modulated RSOA, thus restoring the quality of the encoded pulses.

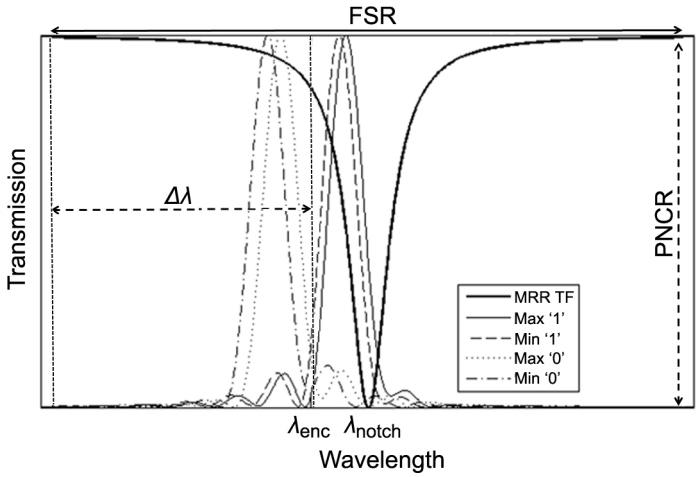

Figure 11. MRR spectral response and action upon spectral components of maximum and minimum encoded logical '1's and '0's at directly modulated RSOA output stream. FSR: free spectral range. PNCR: peak-to-notch contrast ratio. $\Delta\lambda$: detuning (wavelength offset between encoded signal spectral position, λ_{enc}, and shorter sideband transmission peak located FSR/2 away from notch, λ_{notch}).

The MRR target operation wavelengths are those mostly utilized in the applications mentioned at the beginning of the Section 1, that is, in the standard transmission windows of fiber communication systems [57]. Operation at these wavelengths is enabled both by the RSOA broad gain bandwidth and adjustable active medium material composition as well as by the MRR periodic comb-like transmission profile. The latter feature can be exploited provided that the center wavelengths of the encoded data are spaced apart by integer multiples of the free spectral range. In this case, the wavelength allocation should be coarse, in terms of the standardized wavelength division multiplexing grid spacing, or, if a more dense arrangement is desired so as to accommodate more channels, multiple MRRs can be cascaded along the same waveguide bus [64].

The MRR fabrication with regard to (1) size, (2) coupling degree and (3) detuning is technologically feasible according to the following considerations. More specifically: (1) The MRR radius can be down to the very small micrometer scale using high-index contrast waveguide materials [40,65]. (2) The matching between the MRR field transmission coefficient and amplitude attenuation factor for critical coupling is allowed to deviate by 3% from being perfect and still obtain a high PNCR [42]. This is possible by controlling the gap between the straight and bending waveguides using electrically-driven micro-electromechanical system (MEMS) microactuators [66]. (3) The position of the notches relative to the encoded data wavelength can be adjusted by physical means, such as the thermo–optic effect. In this case, electrical heaters are placed in the direct vicinity of the MRR to spectrally shift its resonance [65]. This method is particularly efficient for materials of large positive thermo–optic coefficient, such as silicon, since the required amount of detuning across the FSR can be achieved by supplying an electrical power of the order of a few mWs [65]. Overall, the MRR physical dimensions and tolerances can be determined by modeling the MRR using commercially available simulation software platforms based on coupled mode theory. This procedure is executed for a given waveguide structure material (hence effective index), fabrication technology (hence propagation loss) and incident light (hence wavelength) [67], and has been the subject of research elsewhere, thus being out of the scope of this paper. For example [68], a 20 μm-radius MRR fabricated on a silicon-on-insulator substrate consisting of a 1-μm-thick box layer and 0.45-μm-thick device layer, with waveguide width of 0.5 μm, round-trip propagation losses less than 2 dB/cm and gap between straight and bending waveguide of 250 nm, can efficiently act as notch filter, with PNCR 15 dB, on optical signals centered in the vicinity of 1550 nm.

4. Conclusions

In conclusion, we have demonstrated the capability of an MRR configured as notch filter to bypass the limited modulation bandwidth of an RSOA and directly modulate the RSOA nearly three-and-a-half times faster than possible without the MRR. The analysis of the results obtained through modeling and simulation of the RSOA and MRR response reveals that if the MRR critical parameters are properly selected, which is technologically feasible, then the MRR allows one to enhance the RSOA modulation bandwidth with improved performance and encoded signal characteristics. Employing the MRR in practice allows one to leverage the benefits of free spectral range fine adjustment, controllable finesse, sharp spectral selectivity, feasible and versatile detuning, bandwidth and wavelength tunability, enhanced peak-to-notch contrast ratio, the existence of many different material systems and corresponding fabrication processes, integration compatibility with other photonic devices and platforms, and off-the-shelf availability.

Author Contributions: Zoe V. Rizou and Kyriakos E. Zoiros conceived the paper theme, applied and adapted RSOA and MRR modeling, ran the simulations, derived and interpreted the obtained results and wrote the manuscript.

Conflicts of Interest: The authors declare no conflict of interest.

References

1. Spiekman, L.H. Active devices in passive optical networks. *J. Lightwave Technol.* **2013**, *31*, 488–497.
2. Liu, Z.; Sadeghi, M.; de Valicourt, G.; Brenot, R.; Violas, M. Experimental validation of a reflective semiconductor optical amplifier model used as a modulator in radio over fiber systems. *IEEE Photonics Technol. Lett.* **2011**, *23*, 576–578.
3. Meehan, A.; Connelly, M.J. Experimental characterization and modeling of the improved low frequency response of a current modulated bulk RSOA slow light based microwave phase shifter. *Opt. Commun.* **2015**, *341*, 241–244.
4. Guiying, J.; Lirong, H. Remodulation scheme based on a two-section reflective SOA. *J. Semicond.* **2014**, *35*, 054008.
5. Huang, L.; Hong, W.; Jiang, G. All-optical power equalization based on a two-section reflective semiconductor optical amplifier. *Opt. Express* **2013**, *21*, 4598–4611.
6. Peng, P.C.; Shiu, K.C.; Liu, W.C.; Chen, K.J.; Lu, H.H. A fiber-optical cable television system using a reflective semiconductor optical amplifier. *Laser Phys.* **2013**, *23*, 025106.
7. Connelly, M.J. *Semiconductor Optical Amplifiers*; Kluwer Academic Publishers: Dordrecht, The Netherlands, 2002.
8. König, S. *Semiconductor Optical Amplifiers and mm-Wave Wireless Links for Converged Access Networks*; Karlsruhe Series in Photonics & Communications; Karlsruhe Institute of Technology, Institute of Photonics and Quantum Electronics (IPQ): Karlsruhe, Germany, 2014; Volume 14.
9. Cho, K.Y.; Takushima, Y.; Chung, Y.C. 10-Gb/s operation of RSOA for WDM PON. *IEEE Photonics Technol. Lett.* **2008**, *20*, 1533–1535.
10. Wei, J.L.; Hamié, A.; Gidding, R.P.; Hugues-Salas, E.; Zheng, X.; Mansoor, S.; Tang, J.M. Adaptively modulated optical OFDM modems utilizing RSOAs as intensity modulators in IMDD SMF transmission systems. *Opt. Express* **2010**, *18*, 8556–8573.
11. Shim, H.K.; Kim, H.; Chung, Y.C. 20-Gb/s polar RZ 4-PAM transmission over 20-km SSMF using RSOA and direct detection. *IEEE Photonics Technol. Lett.* **2015**, *27*, 1116–1119.
12. Cho, K.Y.; Choi, B.S.; Takushima, Y.; Chung, Y.C. 25.78-Gb/s operation of RSOA for next-generation optical access networks. *IEEE Photonics Technol. Lett.* **2011**, *23*, 495–497.
13. Schrenk, B.; de Valicourt, G.; Omella, M.; Lazaro, J.A.; Brenot, R.; Prat, J. Direct 10-Gb/s modulation of a single-section RSOA in PONs with high optical budget. *IEEE Photonics Technol. Lett.* **2010**, *22*, 392–394.
14. Rizou, Z.V.; Zoiros, K.E.; Morel, P. Improving SOA direct modulation capability with optical filtering. In Proceedings of the International Conference on Transparent Optical Networks, Trento, Italy, 10–14 July 2016.
15. Papagiannakis, I.; Omella, M.; Klonidis, D.; Birbas, A.N.; Kikidis, J.; Tomkos, I.; Prat, J. Investigation of 10-Gb/s RSOA-based upstream transmission in WDM-PONs utilizing optical filtering and electronic equalization. *IEEE Photonics Technol. Lett.* **2008**, *20*, 2168–2170.

16. Cossu, G.; Bottoni, F.; Corsini, R.; Presi, M.; Ciaramella, E. 40 Gb/s single R-SOA transmission by optical equalization and adaptive OFDM. *IEEE Photonics Technol. Lett.* **2013**, *25*, 2119–2122.
17. Kim, H. 10-Gb/s operation of RSOA using a delay interferometer. *IEEE Photonics Technol. Lett.* **2010**, *22*, 1379–1381.
18. Su, T.; Zhang, M.; Chen, X.; Zhang, Z.; Liu, M.; Liu, L.; Huang, S. Improved 10-Gbps uplink transmission in WDM-PON with RSOA-based colorless ONUs and MZI-based equalizers. *Opt. Laser Technol.* **2013**, *51*, 90–97.
19. Zhang, M.; Wang, D.; Cao, Z.; Chen, X.; Huang, S. Suppression of pattern dependence in 10 Gbps upstream transmission of WDM-PON with RSOA-based ONUs. *Opt. Commun.* **2013**, *308*, 248–252.
20. Presi, M.; Chiuchiarelli, A.; Corsini, R.; Choudury, P.; Bottoni, F.; Giorgi, L.; Ciaramella, E. Enhanced 10 Gb/s operations of directly modulated reflective semiconductor optical amplifiers without electronic equalization. *Opt. Express* **2012**, *20*, B507–B512.
21. Zoiros, K.E.; Morel, P. Enhanced performance of semiconductor optical amplifier at high direct modulation speed with birefringent fiber loop. *AIP Adv.* **2014**, *4*, 077107.
22. Engel, T.; Rizou, Z.V.; Zoiros, K.E.; Morel, P. Semiconductor optical amplifier direct modulation with double-stage birefringent fiber loop. *Appl. Phys. B-Lasers Opt.* **2016**, *122*, 158.
23. Zoiros, K.E.; Morel, P.; Hamze, M. Performance improvement of directly modulated semiconductor optical amplifier with filter-assisted birefringent fiber loop. *Microw. Opt. Technol. Lett.* **2015**, *57*, 2247–2251.
24. Rizou, Z.V.; Zoiros, K.E. Performance analysis and improvement of semiconductor optical amplifier direct modulation with assistance of microring resonator notch filter. *Opt. Quantum Electron.* **2017**, *49*, 119.
25. Katz, O.; Malka, D. Design of novel SOI 1×4 optical power splitter using seven horizontally slotted waveguides. *Photonics Nanostruct.* **2017**, *25*, 9–13.
26. Malka, D.; Cohen, M.; Turkiewicz, J.; Zalevsky, Z. Optical micro-multi-racetrack resonator filter based on SOI waveguides. *Photonics Nanostruct.* **2015**, *16*, 16–23.
27. Antonelli, C.; Mecozzi, A.; Hu, Z.; Santagiustina, M. Analytic study of the modulation response of reflective semiconductor optical amplifiers. *J. Lightwave Technol.* **2015**, *33*, 4367–4376.
28. Stathi, G.; Rizou, Z.V.; Zoiros, K.E. Simulation of directly modulated RSOA. In Proceedings of the International Conference on Numerical Simulation of Optoelectronic Devices, Copenhagen, Denmark, 24–28 July 2017.
29. Connelly, M.J. Reflective semiconductor optical amplifier pulse propagation model. *IEEE Photonics Technol. Lett.* **2012**, *24*, 95–97.
30. Sengupta, I.; Barman, A.D. Analysis of optical re-modulation by multistage modeling of RSOA. *Optik* **2014**, *125*, 3393–3400.
31. Cassioli, D.; Scotti, S.; Mecozzi, A. A time-domain computer simulator of the nonlinear response of semiconductor optical amplifiers. *IEEE J. Quantum Electron.* **2000**, *36*, 1072–1080.
32. Agrawal, G.P.; Olsson, N.A. Self-phase modulation and spectral broadening of optical pulses in semiconductor laser amplifiers. *IEEE J. Quantum Electron.* **1989**, *25*, 2297–2306.
33. Zhou, E.; Zhang, X.; Huang, D. Analysis on dynamic characteristics of semiconductor optical amplifiers with certain facet reflection based on detailed wideband model. *Opt. Express* **2007**, *15*, 9096–9106.
34. Antonelli, C.; Mecozzi, A. Reduced model for the nonlinear response of reflective semiconductor optical amplifiers. *IEEE Photonics Technol. Lett.* **2013**, *25*, 2243–2246.
35. Shen, T.M.; Agrawal, G.P. Pulse-shape effects on frequency chirping in single-frequency semiconductor lasers under current modulation. *J. Lightwave Technol.* **1986**, *4*, 497–503.
36. Cartledge, J.C.; Burley, G.S. The effect of laser chirping on lightwave system performance. *J. Lightwave Technol.* **1989**, *7*, 568–573.
37. Zoiros, K.E.; Botsiaris, C.; Koukourlis, C.S.; Houbavlis, T. Necessary temporal condition for optimizing the switching window of the semiconductor-optical-amplifier-based ultrafast nonlinear interferometer in counter-propagating configuration. *Opt. Eng.* **2006**, *45*, 115005.
38. Ali, M.A.; Elrefaie, A.F.; Ahmed, S.A. Simulation of 12.5 Gb/s lightwave optical time-division multiplexer using semiconductor optical amplifiers as external modulators. *IEEE Photonics Technol. Lett.* **1992**, *4*, 280–283.
39. Chi, J.W.D.; Chao, L.; Rao, M.K. Time-domain large-signal investigation on nonlinear interactions between an optical pulse and semiconductor waveguides. *IEEE J. Quantum Electron.* **2001**, *37*, 1329–1336.
40. Rabus, D.G. *Integrated Ring Resonators: The Compendium*; Spring: Berlin, Germany, 2007.

41. Heebner, J.E.; Wong, V.; Schweinsberg, A.; Boyd, R.W.; Jackson, D.J. Optical transmission characteristics of fiber ring resonators. *IEEE J. Quantum Electron.* **2004**, *40*, 726–730.
42. Absil, P.P.; Hryniewicz, J.V.; Little, B.E.; Wilson, R.A.; Joneckis, L.G.; Ho, P.T. Compact microring notch filters. *IEEE Photonics Technol. Lett.* **2000**, *12*, 398–400.
43. Nielsen, M.L. Experimental and Theoretical Investigation of Semiconductor Optical Amplifier (SOA) Based All-Optical Switches. Ph.D. Thesis, Technical University of Denmark, Lyngby, Denmark, 2004.
44. Pile, B.; Taylor, G. Small-signal analysis of microring resonator modulators. *Opt. Express* **2014**, *22*, 14913–14928.
45. Sato, K.; Toba, H. Reduction of mode partition noise by using semiconductor optical amplifiers. *IEEE J. Sel. Top. Quantum Electron.* **2001**, *7*, 328–333.
46. Ahmed, M.; Lafi, A.E. Analysis of small-signal intensity modulation of semiconductor lasers taking account of gain suppression. *Pramana-J. Phys.* **2008**, *71*, 99–115.
47. Corless, R.M.; Gonnet, G.H.; Hare, D.E.; Jeffrey, D.J.; Knuth, D.E. On the Lambert W function. *Adv. Comput. Math.* **1996**, *5*, 329–359.
48. Dawson, H.G. On the Numerical Value of $\int_0^h e^{x^2} dx$. *Proc. Lond. Math. Soc.* **1897**, *1*, 519–522.
49. Totović, A.R.; Crnjanski, J.V.; Krstić, M.M.; Gvozdić, D.M. Numerical study of the small-signal modulation bandwidth of reflective and traveling-wave SOAs. *J. Lightwave Technol.* **2015**, *33*, 2758–2764.
50. De Valicourt, G.; Pommereau, F.; Poingt, F.; Lamponi, M.; Duan, G.; Chanclou, P.; Violas, M.; Brenot, R. Chirp reduction in directly modulated multi-electrode RSOA devices in passive optical networks. *IEEE Photonics Technol. Lett.* **2010**, *22*, 1425–1427.
51. Zoiros, K.E.; Rizou, Z.V.; Connelly, M.J. On the compensation of chirp induced from semiconductor optical amplifier on RZ data using optical delay interferometer. *Opt. Commun.* **2011**, *284*, 3539–3547.
52. Liu, F.; Wang, T.; Qiang, L.; Ye, T.; Zhang, Z.; Qiu, M.; Su, Y. Compact optical temporal differentiator based on silicon microring resonator. *Opt. Express* **2008**, *16*, 15880–15886.
53. Trebino, R. *Frequency-Resolved Optical Gating: The Measurement of Ultrashort Laser Pulses*; Springer Science & Business Media: New York, NY, USA, 2012; pp. 11–35.
54. Azaña, J.; Park, Y.; Li, F. Linear self-referenced complex-field characterization of fast optical signals using photonic differentiation. *Opt. Commun.* **2011**, *284*, 3772–3784.
55. Watts, R.T.; Shi, K.; Barry, L.P. Time-resolved chirp measurement for 100GBaud test systems using an ideal frequency discriminator. *Opt. Commun.* **2012**, *285*, 2039–2043.
56. Ruege, A.C. Electro-Optic Ring Resonators in Integrated Optics for Miniature Electric Field Sensors. Ph.D. Thesis, The Ohio State University, Columbus, OH, USA, 2001.
57. Agrawal, G.P. *Fiber-Optic Communication Systems*; Wiley: New York, NY, USA, 2002.
58. Wei, J.L.; Hamié, A.; Giddings, R.P.; Tang, J.M. Semiconductor optical amplifier-enabled intensity modulation of adaptively modulated optical OFDM signals in SMF-based IMDD systems. *J. Lightwave Technol.* **2009**, *27*, 3678–3688.
59. Rizou, Z.V.; Zoiros, K.E.; Hatziefremidis, A. Signal amplitude and phase equalization technique for free space optical communications. In Proceedings of the International Conference on Transparent Optical Networks, Cartagena, Spain, 23–27 July 2013.
60. Vardakas, J.S.; Zoiros, K.E. Performance investigation of all-optical clock recovery circuit based on Fabry-Pérot filter and semiconductor optical amplifier assisted Sagnac switch. *Opt. Eng.* **2007**, *46*, 085005.
61. Zoiros, K.E.; Vardakas, J.S.; Tsigkas, M. Study on the instantaneous frequency deviation of pulses switched from semiconductor optical amplifier–assisted Sagnac interferometer. *Opt. Eng.* **2010**, *49*, 075003.
62. Hinton, K.; Stephens, T. Modeling high-speed optical transmission systems. *IEEE J. Sel. Area Commun.* **1993**, *11*, 380–392.
63. Müller, J.; Merget, F.; Azadeh, S.S.; Hauck, J.; García, S.R.; Shen, B.; Witzens, J. Optical peaking enhancement in high-speed ring modulators. *Sci. Rep.* **2014**, *4*, 6310.
64. Padmaraju, K.; Bergman, K. Resolving the thermal challenges for silicon microring resonator devices. *Nanophotonics* **2014**, *3*, 269–281.
65. Bogaerts, W.; De Heyn, P.; Van Vaerenbergh, T.; De Vos, K.; Kumar Selvaraja, S.; Claes, T.; Dumon, P.; Bienstman, P.; Van Thourhout, D.; Baets, R. Silicon microring resonators. *Laser Photonics Rev.* **2012**, *6*, 47–73.
66. Lee, M.C.; Wu, M.C. MEMS-actuated microdisk resonators with variable power coupling ratios. *IEEE Photonics Technol. Lett.* **2005**, *17*, 1034–1036.

67. Stoffer, R.; Hiremath, K.R.; Hammer, M.; Prkna, L.; Čtyrokỳ, J. Cylindrical integrated optical microresonators: Modeling by 3-D vectorial coupled mode theory. *Opt. Commun.* **2005**, *256*, 46–67.
68. Niehusmann, J.; Vörckel, A.; Bolivar, P.H.; Wahlbrink, T.; Henschel, W.; Kurz, H. Ultrahigh-quality-factor silicon-on-insulator microring resonator. *Opt. Lett.* **2004**, *29*, 2861–2863.